

IGA-ODIL: Optimizing DIscrete robust Loss with Isogeometric Analysis to solve forward and inverse problems faster using machine learning tools.

Maciej Paszyński, Tomasz Służalec

Faculty of Computer Science, AGH University of Krakow, Poland

Abstract

Physics-informed neural networks (PINNs) formulate the solution of partial differential equations as residual minimization problems over neural network parameterizations. Although highly flexible, optimization of PINNs using modern variants of Stochastic Gradient Descent algorithms is expensive. On the other hand, iterative computation of PINN parameterization using the Gauss-Newton method suffers from convergence difficulties, dense Jacobian structures, and poor conditioning that limit the effectiveness of second-order optimization methods. In this work, we introduce IGA-ODIL, a spline-based residual minimization framework combining ideas from Optimizing DIscrete Loss (ODIL), robust variational residual minimization, and Isogeometric Analysis (IGA). Instead of neural-network parameterizations of PINNs, the unknown solution is represented by smooth B-spline basis functions, leading to sparse structured Jacobians and efficient Gauss-Newton optimization. We also derive robust residual formulations based on weighted Gram operators, making the loss function related with the true error. The resulting systems inherit locality, sparsity, and approximation-theoretic properties of classical finite element and isogeometric methods while preserving the residual-learning philosophy of scientific machine learning. The proposed methodology is evaluated on several benchmark problems, including Poisson equations, convection-dominated advection-diffusion equations, Helmholtz problems with highly oscillatory solutions, nonlinear Allen-Cahn equations, and inverse Helmholtz parameter identification.

Numerical experiments demonstrate orders-of-magnitude speedups compared with PINNs and CRVPINNs while maintaining high accuracy and robustness.

Keywords: Physics-informed neural networks, Isogeometric analysis, Residual minimization, Gauss–Newton methods, Scientific machine learning, PDE-constrained optimization

1. Introduction

Scientific machine learning has recently emerged as a rapidly developing research direction at the intersection of numerical analysis, partial differential equations (PDEs), optimization, and machine learning. Among the most influential approaches are Physics-Informed Neural Networks (PINNs), introduced by Raissi, Perdikaris, and Karniadakis [1]. PINNs formulate the numerical solution of PDEs as residual minimization problems in which the unknown solution is represented by a neural network and the governing equations are enforced through collocation-based residual losses. Numerous extensions and variants have appeared, including Variational PINNs (VPINNs) [9], Deep Ritz methods [10], adaptive and domain-decomposition formulations, as well as operator-learning approaches such as Fourier Neural Operators [21]. More general overviews of scientific machine learning and physics-informed learning frameworks can be found in [20]. Recent applications show that PINNs are used particularly often in fluid mechanics, where they support flow reconstruction, inverse parameter identification, and data assimilation from sparse or noisy measurements [2]. They have been applied to wake flows, biomedical flows, supersonic flows, and experimental stratified flows, demonstrating their potential for combining measurement data with Navier–Stokes-type models [2, 6]. PINNs have been used for heat transfer in porous media, where they can estimate temperature fields, heat fluxes, and effective thermal conductivity without requiring dense labeled data [3]. They have also been applied to two-phase flow and heat transfer problems, where the physics-informed loss helps enforce the governing equations while learning from simulation data [4]. More recently, PINNs have

been considered as components of digital twins, where the goal is to combine sensor data, reduced-order modeling, and physical constraints for real-time prediction and uncertainty-aware monitoring [5].

Despite their flexibility, PINNs suffer from several important numerical and theoretical difficulties. Optimization landscapes associated with deep neural-network parameterizations are highly nonconvex and frequently exhibit poor conditioning, flat directions, vanishing gradients, and parameter symmetries [8]. As a consequence, first-order optimization methods such as stochastic gradient descent (SGD) and Adam [24] often converge slowly and unreliably. Furthermore, second-order methods such as Newton or Gauss–Newton optimization are difficult to apply effectively because the resulting Jacobians are typically large, dense, and ill-conditioned [19].

An additional difficulty is that the classical PINN residual loss generally lacks robustness with respect to physically meaningful norms. In many cases, the residual loss does not accurately represent the discretization error measured in Sobolev norms, leading to poor correlation between optimization convergence and physical solution quality [11]. This observation motivated the development of Robust Variational PINNs [11], based on the weak residuals of Variational PINNs (VPINNs) [9]. Additionally, to speed up the loss estimation, Collocation-based Robust Variational Physics-Informed Neural Networks (CRVPINNs) [12] have been recently proposed. In particular, the robust loss takes the form

$$\Phi(u) = R(u)^T G^{-1} R(u), \quad (1)$$

where G is a Gram matrix associated with a suitable variational inner product [11], and $R(u)$ is a weak residual in the case of VPINNs or a discrete weak residual (computed with Kronecker product delta test functions) in the case of CRVPINNs. Although robust residual formulations improve the stability of PINN losses, the optimization challenges associated with deep nonlinear parameterizations remain. Neural-network Jacobians remain globally coupled and dense, limiting the scalability and effectiveness of second-order optimization methods.

A complementary research direction was recently proposed by Karnakov, Litvinov, and Koumoutsakos through the Optimizing DIscrete Loss (ODIL) framework [13]. The central idea of ODIL is that residual minimization does not fundamentally require neural-network parameterizations. Instead, the unknown solution is represented directly through discrete degrees of freedom optimized using PDE residual losses. ODIL demonstrated that many scientific machine learning ideas can be interpreted as optimization-based PDE discretizations rather than purely neural-network methods. ODIL interprets PDE solving as optimization over discrete degrees of freedom using residual losses evaluated at collocation points. The resulting formulation preserves many advantages of scientific machine learning, including natural extensions to inverse problems and PDE-constrained optimization.

However, point-based ODIL discretizations are not globally continuous like neural network representations. They also lack several important properties associated with classical spline and finite element approximation spaces. In particular, point-value parameterizations do not naturally provide high-order smoothness, compactly supported basis functions, and approximation-theoretic properties associated with spline spaces and classical Galerkin discretizations [18].

Isogeometric Analysis, introduced by Hughes, Cottrell, and Bazilevs [14], establishes spline-based discretizations as powerful alternatives to classical finite element methods. B-splines and NURBS provide smooth, high-order approximation spaces with excellent approximation properties, sparse local support, and direct compatibility with CAD geometries [14, 15, 16, 25, 26]. Recent applications of isogeometric analysis (IGA) show that it is widely used in problems where smoothness, high-order accuracy, and exact geometry representation are important. In fracture mechanics, IGA has been applied to phase-field models of brittle, anisotropic, and polycrystalline fracture, where the higher continuity of spline spaces is advantageous for fourth-order and gradient-enhanced formulations [30, 31, 32, 38]. Another active direction is design and topology optimization, where the common representation of geometry and analysis fields supports design-through-analysis workflows [33]. Recent developments also extend

IGA to complex CAD geometries using analysis-suitable T-splines and G-spline surfaces [34, 35]. In fluid mechanics and aerodynamics, IGA has been used for turbulent flows, moving domains, fluid–structure interaction, and space–time simulations of complex engineering configurations [36, 40]. Applications in biomechanics include cardiac electrophysiology and ventricular mechanics, where smooth patient-specific geometries and coupled multiphysics models are essential [37, 39].

We propose an unified framework IGA-ODIL. The proposed methodology replaces neural-network parameterizations with smooth B-spline approximation spaces while preserving the residual-minimization philosophy of scientific machine learning. Specifically, the unknown solution is represented as

$$u_h(x, y) = \sum_{i=1}^{N_x} \sum_{j=1}^{N_y} c_{ij} B_i^{(p)}(x) B_j^{(q)}(y), \quad (2)$$

where the trainable variables are spline coefficients rather than neural-network parameters. The key observation of this work is that spline parameterizations fundamentally alter the structure of residual minimization problems. The Jacobian of spline discretization inherits the sparse locality structure of classical PDE discretizations. Consequently, the Gauss–Newton systems become sparse and structured; second-order optimization becomes computationally tractable; least-squares PDE structure reappears; and locality and scalability are recovered. In contrast to neural-network parameterizations, spline spaces therefore restore many advantages of classical numerical PDE methods while preserving the optimization-based residual-learning formulation characteristic of scientific machine learning. The proposed framework additionally incorporates robust variational residual formulations using weighted Gram operators. The resulting method combines robust residual minimization, smooth spline approximation, sparse Gauss-Newton optimization, PDE-constrained inverse optimization, and scientific machine learning formulations.

The methodology is evaluated on several benchmark problems, including Poisson equations, the Eriksson-Johnson model problem, high-frequency Helmholtz

problems, nonlinear Allen–Cahn equations, and PDE-constrained inverse problems. The numerical experiments demonstrate substantial computational advantages compared with PINNs and CRVPINNs, including orders-of-magnitude speedups while maintaining high approximation quality and robustness.

The remainder of the paper is organized as follows. Section 2 reviews robust residual minimization and Gauss–Newton optimization for PINNs. Section 3 reformulates the ODIL method for the robust loss case. Section 4 introduces the IGA-ODIL formulation for robust loss and it derives the corresponding sparse Gauss–Newton systems. Section 5 presents numerical experiments for forward PDE benchmarks, including Poisson, advection-diffusion, Helmholtz, and Allen–Cahn problems. Section 6 considers PDE-constrained inverse problems. We conclude the paper in Section 7. We also include an Appendix A with code references and Appendix B with proof of convergence.

2. PINNs and Robust Residual Minimization

2.1. PINN and CRVPINN formulations

Consider a PDE operator

$$\mathcal{L}u = f \tag{3}$$

in a domain Ω . PINNs approximate the solution using a neural network,

$$u_\theta(x, y) = \text{NN}(x, y) = \sigma(A_n \sigma(\dots \sigma(A_1 \begin{bmatrix} x \\ y \end{bmatrix} + \beta_1) \dots) + \beta_n) \tag{4}$$

where A_i are layer weights, σ are nonlinear activation functions, and β_i are biases. In general, $\theta \in \mathbb{R}^P$ denotes the trainable parameters [1]. The PINN method is summarized in Figure 1. The residual evaluated at collocation points $\{\mathbf{x}_k\}_{k=1}^M$ is

$$R_k(\theta) = \mathcal{L}u_\theta(\mathbf{x}_k) - f(\mathbf{x}_k). \tag{5}$$

The classical PINN loss

$$\mathcal{J}(\theta) = \frac{1}{2} \sum_{k=1}^M |R_k(\theta)|^2. \tag{6}$$

can be interpreted as a nonlinear least-squares optimization problem over neural-network parameterizations [10, 19]. The classical way of solving the PINN problem is through some modern variants of the Stochastic Gradient Descent method. The ADAM algorithm [24], which replaces the local gradient with the weighted average gradient from several previous iterations, is one of the most popular choices. The method is summarized in Algorithm 1. PINNs

Algorithm 1 Physics-Informed Neural Network (PINN)

- 1: Construct neural network approximation $u_\theta(\mathbf{x})$
 - 2: Select collocation points $\{\mathbf{x}_k\}_{k=1}^M$
 - 3: Initialize network parameters $\theta^{(0)}$
 - 4: **while** not converged **do**
 - 5: Evaluate residuals at collocation points $R_k(\theta^{(n)}) = \mathcal{L}u_{\theta^{(n)}}(\mathbf{x}_k) - f(\mathbf{x}_k), \quad k = 1, \dots, M$
 - 6: Form residual vector $R(\theta^{(n)}) = [R_1(\theta^{(n)}), \dots, R_M(\theta^{(n)})]^T$
 - 7: Compute PINN loss $\mathcal{J}(\theta^{(n)}) = \frac{1}{2} \sum_{k=1}^M |R_k(\theta^{(n)})|^2 + \mathcal{L}_{BC}$
 - 8: Compute gradients $\nabla_\theta \mathcal{J}(\theta^{(n)})$ using backpropagation and automatic differentiation
 - 9: Update neural-network parameters $\theta^{(n+1)} = \theta^{(n)} - \eta \nabla_\theta \mathcal{J}(\theta^{(n)})$ using Adam, L-BFGS, or related optimizers
 - 10: **end while**
-

solved with SGD/ADAM methods are generally computationally much more demanding than Finite Element Method/Isogeometric Analysis solvers.

2.2. Gauss-Newton Optimization for PINNs

An alternative way to compute θ coefficients of neural network approximation may be the application of second order optimization methods like the Gauss-Newton. We can derive the Gauss-Newton method for solving the residual minimization problem when the solution is represented by NN. Let $u_\theta(\mathbf{x})$ denote NN parameterized by $\theta \in \mathbb{R}^P$ (composition of affine transformations and

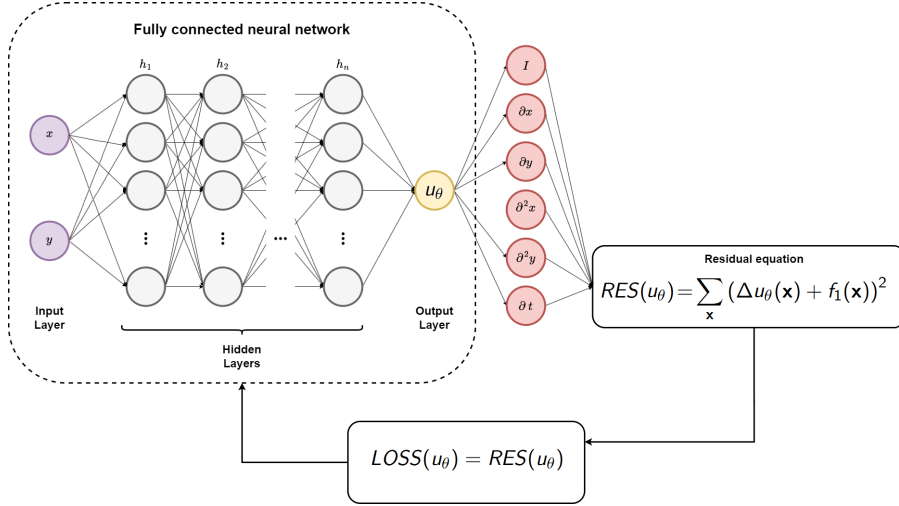


Figure 1: PINN (Physics Informed Neural Networks)

nonlinear activation functions). The PDE residual is given by

$$R_k(\theta) = \mathcal{L}u_\theta(\mathbf{x}_k) - f(\mathbf{x}_k), \quad (7)$$

and evaluated at a set of collocation points $\{\mathbf{x}_k\}_{k=1}^M$:

$$R(\theta) = (R_1(\theta), \dots, R_M(\theta))^T = (R(\mathbf{x}_1; \theta), \dots, R(\mathbf{x}_M; \theta))^T \in \mathbb{R}^M. \quad (8)$$

The objective is to minimize the nonlinear least-squares functional

$$\mathcal{J}(\theta) = \frac{1}{2} \|R(\theta)\|_2^2. \quad (9)$$

The Jacobian matrix is defined as

$$J(\theta) = \frac{\partial R(\theta)}{\partial \theta} \in \mathbb{R}^{M \times P}. \quad (10)$$

(here $M = \#$ collocation points, $P = \#$ NN parameters) Using the chain rule, each row of $J(\theta)$ (single point) is given by

$$\frac{\partial R(\mathbf{x}_k; \theta)}{\partial \theta} = \frac{\partial}{\partial \theta} (\mathcal{L}u_\theta(\mathbf{x}_k)) = \mathcal{L} \left(\frac{\partial u_\theta(\mathbf{x}_k)}{\partial \theta} \right). \quad (11)$$

The term $\frac{\partial u_\theta(\mathbf{x})}{\partial \theta}$ can be computed efficiently using backpropagation. At an iterate $\theta^{(k)}$, we linearize the residual

$$R(\theta^{(k)} + \delta) \approx R(\theta^{(k)}) + J(\theta^{(k)})\delta. \quad (12)$$

The Gauss-Newton step is obtained by minimizing the quadratic model

$$\min_{\delta} \|R(\theta^{(k)}) + J(\theta^{(k)})\delta\|_2^2. \quad (13)$$

This leads to the normal equations

$$J(\theta^{(k)})^T J(\theta^{(k)}) \delta^{(k)} = -J(\theta^{(k)})^T R(\theta^{(k)}). \quad (14)$$

The parameters are updated as follows:

$$\theta^{(k+1)} = \theta^{(k)} + \delta^{(k)}. \quad (15)$$

The method is summarized in Algorithm 2. Such formulations correspond

Algorithm 2 Gauss–Newton Training of Physics-Informed Neural Networks

- 1: Construct neural network approximation $u_{\theta}(\mathbf{x})$
 - 2: Select collocation points $\{\mathbf{x}_k\}$
 - 3: Initialize network parameters $\theta^{(0)}$
 - 4: **while** not converged **do**
 - 5: Evaluate residual vector $R(\theta^{(k)}) = [R(\mathbf{x}_1; \theta^{(k)}), \dots, R(\mathbf{x}_{N_r}; \theta^{(k)})]^T$
 - 6: Assemble Jacobian matrix $J(\theta^{(k)}) = \frac{\partial R(\theta^{(k)})}{\partial \theta}$ using automatic differentiation
 - 7: Solve the Gauss–Newton system $(J^T J) \delta^{(k)} = -J^T R$
 - 8: Update neural network parameters $\theta^{(k+1)} = \theta^{(k)} + \delta^{(k)}$
 - 9: **end while**
-

to nonlinear least-squares optimization methods [19]. However, the Jacobian $J(\theta)$ is typically large and dense, and the resulting systems are large and ill-conditioned. Neural-network Jacobians are typically dense, highly nonlinear, and poorly conditioned [8]. In practice, the resulting systems are often singular or numerically unstable, limiting the applicability of second-order optimization methods for large-scale PINN formulations.

2.3. Gauss–Newton Optimization for CRVPINNs

Classical residual losses employed by PINNs are generally not equivalent to physically meaningful energy norms [11]. Robust variational residual minimiza-

tion introduces weighted losses of the form

$$\Phi(u) = \frac{1}{2}R(u)^T G^{-1}R(u), \quad (16)$$

where G is a symmetric positive definite Gram matrix associated with a variational inner product [11, 12]. Following the discrete weak formulation described in [12] we have

$$\frac{1}{\mu}\sqrt{\Phi(u)} \leq \|u - u_{exact}\|_{\nabla, h} \leq \frac{1}{\alpha}\sqrt{\Phi(u)}. \quad (17)$$

Thus, the robust loss becomes equivalent to the discretization of the true error measured in suitable discrete Sobolev norms [12]. Classical way of solving CRVPINNs is using Stochastic Gradient Descent or ADAM [24] method. We can also derive the Gauss-Newton method for solving the residual minimization problem when the solution is represented by CRVPINN. Let $u_\theta(x)$ denote a neural network parameterized by $\theta \in \mathbb{R}^P$. The PDE residual is defined as

$$R(x; \theta) = \mathcal{L}u_\theta(x) - f(x), \quad (18)$$

and evaluated at collocation points $\{x_k\}_{k=1}^M$:

$$R(\theta) = (R(x_1; \theta), \dots, R(x_M; \theta))^T \in \mathbb{R}^M. \quad (19)$$

Unlike standard PINNs, CRVPINNs employ weighted or norm-equivalent residual minimization to improve stability and convergence properties. The objective is to minimize the robust least-squares functional

$$\mathcal{J}(\theta) = \frac{1}{2}R(\theta)^T G^{-1}R(\theta), \quad (20)$$

where G is a Gram matrix associated with a suitable Sobolev or energy norm.

The Jacobian matrix is defined as

$$J(\theta) = \frac{\partial R(\theta)}{\partial \theta} \in \mathbb{R}^{M \times P}. \quad (21)$$

(M = number of collocation points, P = number of NN parameters)

Using the chain rule,

$$\frac{\partial R(x_k; \theta)}{\partial \theta} = \frac{\partial}{\partial \theta} (\mathcal{L}u_\theta(x_k)) = \mathcal{L} \left(\frac{\partial u_\theta(x_k)}{\partial \theta} \right). \quad (22)$$

At iteration $\theta^{(k)}$, we linearize the residual:

$$R(\theta^{(k)} + \delta) \approx R(\theta^{(k)}) + J(\theta^{(k)})\delta. \quad (23)$$

The Gauss-Newton step minimizes the quadratic model

$$\min_{\delta} \|G^{-1/2}(R + J\delta)\|_2^2. \quad (24)$$

This leads to the weighted normal equations:

$$J^T G^{-1} J \delta^{(k)} = -J^T G^{-1} R. \quad (25)$$

The parameters are updated by

$$\theta^{(k+1)} = \theta^{(k)} + \delta^{(k)}. \quad (26)$$

The method is summarized in Algorithm 3. However, unlike spline discretizations, the Jacobian $J(\theta)$ is typically large and dense, and the weighted Hessian approximation $J^T G^{-1} J$

3. ODIL and Fast Robust Residual Minimization

3.1. ODIL formulation

In the ODIL (Optimizing DIscrete Loss) method, the unknown solution is represented directly by discrete values at collocation points. For the Poisson equation, we introduce a structured set of collocation points $\{(x_i, y_j)\}_{i=1, j=1}^{N_x, N_y}$, and define the unknown discrete solution values $u_{i,j} \approx u(x_i, y_j)$. The trainable variables are, therefore, the nodal unknowns $u \in \mathbb{R}^{N_x \times N_y}$. The PDE residual is evaluated directly at collocation points. For example, using a standard five-point discretization of the Laplacian,

$$R_{i,j}(u) = \frac{u_{i+1,j} - 2u_{i,j} + u_{i-1,j}}{h_x^2} + \frac{u_{i,j+1} - 2u_{i,j} + u_{i,j-1}}{h_y^2} + f(x_i, y_j). \quad (27)$$

The residual vector is obtained by stacking all local residuals: $R(u) = [R_{1,1}(u), \dots, R_{N_x, N_y}(u)]^T$. The ODIL loss functional is defined as the discrete residual minimization problem

Algorithm 3 Gauss–Newton Optimization for CRVPINNs

- 1: Construct neural network approximation $u_\theta(\mathbf{x})$
 - 2: Select collocation points $\{\mathbf{x}_k\}$
 - 3: Assemble Gram matrix G
 - 4: Compute LU factorization once: $G = LU$
 - 5: Initialize network parameters $\theta^{(0)}$
 - 6: **while** not converged **do**
 - 7: Evaluate residual vector $R(\theta^{(k)}) = [R(\mathbf{x}_1; \theta^{(k)}), \dots, R(\mathbf{x}_{N_r}; \theta^{(k)})]^T$
 - 8: Assemble the Jacobian matrix $J(\theta^{(k)}) = \frac{\partial R(\theta^{(k)})}{\partial \theta} \in \mathbb{R}^{N_r \times P}$ using automatic differentiation
 - 9: Solve $LU y_R = R$
 - 10: Compute weighted Jacobian $LU Y_J = J$ where each column of Y_J is obtained by solving $LU y_j = J_j$ with J_j denoting the j -th column of J
 - 11: Assemble Gauss–Newton Hessian approximation $H = J^T Y_J$
 - 12: Assemble right-hand side $g = J^T y_R$
 - 13: Solve the linearized system $H \delta^{(k)} = -g$
 - 14: Update neural network parameters $\theta^{(k+1)} = \theta^{(k)} + \delta^{(k)}$
 - 15: **end while**
-

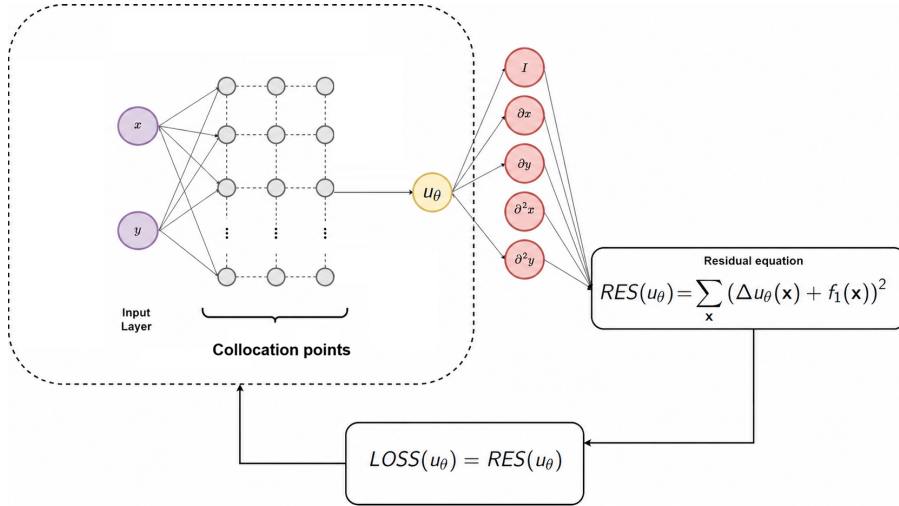


Figure 2: ODIL (Optimizing Discrete Loss)

$$LOSS(u) = \|R(u)\|^2 = \sum_{i,j} R_{i,j}(u)^2. \quad (28)$$

To improve robustness and discretization invariance, we introduce the weighted residual functional

$$\Phi(u) = \frac{1}{2} R(u)^T G^{-1} R(u), \quad (29)$$

where G denotes the Gram matrix associated with the residual representation.

3.2. Gauss–Newton Optimization for ODIL

Using the first-order linearization $R(u + \delta) \approx R + J\delta$, where $J(u) = \frac{\partial R(u)}{\partial u}$, the robust functional becomes

$$\Phi(u + \delta) = \frac{1}{2} (R + J\delta)^T G^{-1} (R + J\delta). \quad (30)$$

Expanding the quadratic form yields

$$\Phi(u + \delta) = \frac{1}{2} (R^T G^{-1} R + 2\delta^T J^T G^{-1} R + \delta^T J^T G^{-1} J\delta). \quad (31)$$

Differentiating with respect to δ gives

$$\nabla_{\delta} \Phi = J^T G^{-1} R + J^T G^{-1} J\delta. \quad (32)$$

Setting the gradient to zero produces the weighted Gauss–Newton equations

$$(J^T G^{-1} J)\delta = -J^T G^{-1} R. \quad (33)$$

For linear PDEs, the residual has the affine form $R(u) = Au - b$, which implies $J = A$. Consequently, the Gauss–Newton method reduces to the solution of a weighted least-squares discretization. To avoid explicit formation of G^{-1} , the Gram matrix is factorized once $G = LU$. Applications of G^{-1} are then replaced by triangular solves. The resulting ODIL method is summarized in Algorithm 4.

Algorithm 4 Gauss–Newton Optimization for ODIL

- 1: Construct collocation points $\{\mathbf{x}_{i,j}\}$
 - 2: Initialize discrete solution values $u^{(0)}$
 - 3: Assemble Gram matrix G
 - 4: Compute LU factorization once: $G = LU$
 - 5: **while** not converged **do**
 - 6: Evaluate residual vector $R(u^{(k)})$
 - 7: Assemble Jacobian matrix $J(u^{(k)}) = \frac{\partial R(u^{(k)})}{\partial u}$
 - 8: Solve $LU y_R = R$
 - 9: Compute weighted Jacobian $LU Y_J = J$ where each column of Y_J is obtained by solving $LU y_j = J_j$ with J_j denoting the j -th column of J
 - 10: Assemble Gauss–Newton Hessian approximation $H = J^T Y_J$
 - 11: Assemble right-hand side $g = J^T y_R$
 - 12: Solve the linearized system $H \delta^{(k)} = -g$
 - 13: Update solution $u^{(k+1)} = u^{(k)} + \delta^{(k)}$
 - 14: **end while**
-

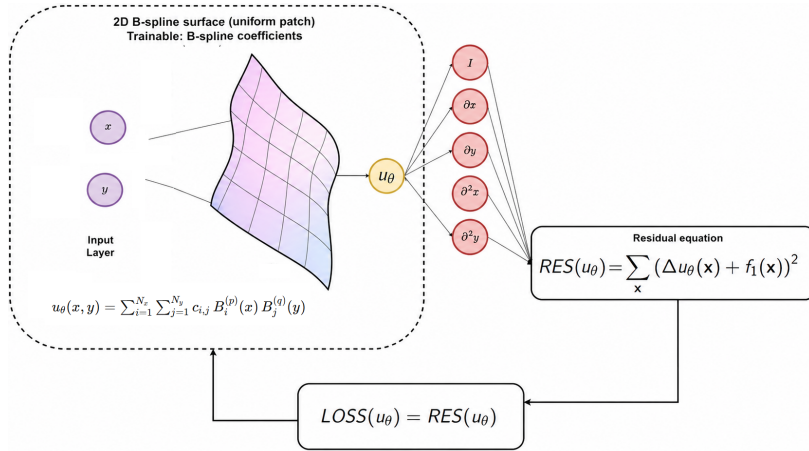


Figure 3: IGA-ODIL (Isogeometric Analysis by Optimizing DIscrete Loss)

4. IGA-ODIL and fast Robust Residual Minimization

4.1. IGA-ODIL formulation

In the IGA-ODIL method, the unknown solution is represented using tensor-product B-splines. For example, for the Poisson equation,

$$u_c(x, y) = \sum_{i=1}^{N_x} \sum_{j=1}^{N_y} c_{i,j} B_i^{(p)}(x) B_j^{(q)}(y), \quad c \in \mathcal{M}^{N_x \times N_y} \quad (34)$$

$$R(u_c) = \sum_{\hat{x}, \hat{y}} \left(\frac{\partial^2 u_c(\hat{x}, \hat{y})}{\partial x^2} + \frac{\partial^2 u_c(\hat{x}, \hat{y})}{\partial y^2} + f(\hat{x}, \hat{y}) \right)^2 \quad (35)$$

$$= \sum_{\hat{x}, \hat{y}} \left(\sum_{i=1}^{N_x} \sum_{j=1}^{N_y} c_{i,j} \left[\frac{\partial^2 B_i^{(p)}(\hat{x})}{\partial x^2} B_j^{(q)}(\hat{y}) + B_i^{(p)}(\hat{x}) \frac{\partial^2 B_j^{(q)}(\hat{y})}{\partial y^2} \right] + f(\hat{x}, \hat{y}) \right)^2 \quad (36)$$

The trainable variables are the spline coefficients c . In general, the residual evaluated at collocation points (\hat{x}_k, \hat{y}_k) is

$$R_k(c) = \mathcal{L}u_c(\hat{x}_k, \hat{y}_k) - f(\hat{x}_k, \hat{y}_k). \quad (37)$$

The robust residual functional is given by

$$\Phi(u) = \frac{1}{2} R(u)^T G^{-1} R(u). \quad (38)$$

4.2. Gauss-Newton Optimization for IGA-ODIL

Using the linearization $R(u + \delta) \approx R + J\delta$, the robust functional

$$\Phi(u + \delta) = \frac{1}{2} (R + J\delta)^T G^{-1} (R + J\delta). \quad (39)$$

$$\Phi(u + \delta) = \frac{1}{2} (R^T G^{-1} R + 2\delta^T J^T G^{-1} R + \delta^T J^T G^{-1} J \delta). \quad (40)$$

Differentiating with respect to δ gives $\nabla_\delta \Phi = J^T G^{-1} R + J^T G^{-1} J \delta$. Setting the gradient to zero yields the weighted normal equations:

$$(J^T G^{-1} J) \delta = -J^T G^{-1} R \quad (41)$$

To solve (41), we require the Jacobian of the residual with respect to the coefficients,

$$J(c) = \frac{\partial R(c)}{\partial c}. \quad (42)$$

For linear PDEs the residual has the affine form $R(c) = Ac - b$, which implies $J = A$. Consequently, Gauss–Newton becomes equivalent to solving a least-squares PDE discretization. The overall method for solving IGA–ODIL is summarized in Algorithm 5.

Algorithm 5 Gauss–Newton Optimization for IGA–ODIL

- 1: Construct tensor-product B-spline basis functions $\{\phi_{i,j}(x,y)\} = \{B_i^{(p)}(x)B_j^{(q)}(y)\}$
 - 2: Select collocation points $\{\mathbf{x}_k\}$
 - 3: Initialize spline coefficients $c^{(0)}$
 - 4: Assemble Gram matrix G
 - 5: Compute LU factorization once: $G = LU$
 - 6: **while** not converged **do**
 - 7: Evaluate spline solution $u_h^{(k)}(x,y) = \sum_{i=1}^{N_x} \sum_{j=1}^{N_y} c_{i,j}^{(k)} B_i^{(p)}(x) B_j^{(q)}(y)$
 - 8: Evaluate residual vector $R(c^{(k)})$
 - 9: Assemble Jacobian matrix $J(c^{(k)}) = \frac{\partial R(c^{(k)})}{\partial c}$
 - 10: Solve $LU y_R = R$
 - 11: Compute weighted Jacobian $LU Y_J = J$ where each column of Y_J is obtained from $LU y_j = J_j$ with J_j denoting the j -th column of J
 - 12: Assemble Gauss–Newton Hessian approximation $H = J^T Y_J$
 - 13: Assemble right-hand side $g = J^T y_R$
 - 14: Solve the linearized system $H \delta^{(k)} = -g$
 - 15: Update spline coefficients $c^{(k+1)} = c^{(k)} + \delta^{(k)}$
 - 16: **end while**
-

5. Numerical Experiments

In this section, we compare the PINN, CRVPINN, ODIL, and IGA-ODIL methods on a number of benchmarks.

5.1. Poisson Problem

We first consider the Poisson equation

$$-\Delta u = f \quad (43)$$

with manufactured solution

$$u(x, y) = \sin(2\pi x) \sin(2\pi y). \quad (44)$$

The corresponding forcing term is

$$f(x, y) = 8\pi^2 \sin(2\pi x) \sin(2\pi y). \quad (45)$$

Figure 4 illustrates the discrepancy between the classical PINN residual loss and the true H^1 error.



Figure 4: PINN residual loss versus true error for the Poisson benchmark.

The robust CRVPINN formulation using the robust loss and discrete weak formulations substantially improves convergence robustness, see Figure 5. The

training time using the ADAM algorithm with 100×100 collocation points and 2 fully connected neural network layers is 6 min and 51 sec on Google Compute Engine GPU. Replacing the ADAM method with the Gauss-Newton formulation with Neural Network parameterization results in lack of convergence

```

Residual size: 1600
Parameter size: 1801
Epoch 0 | Loss = 1.481357e+03 | time = 22.62s
Residual size: 1600
Parameter size: 1801
_LinAlgError: torch.linalg.solve: The solver failed because the
input matrix is singular.

```

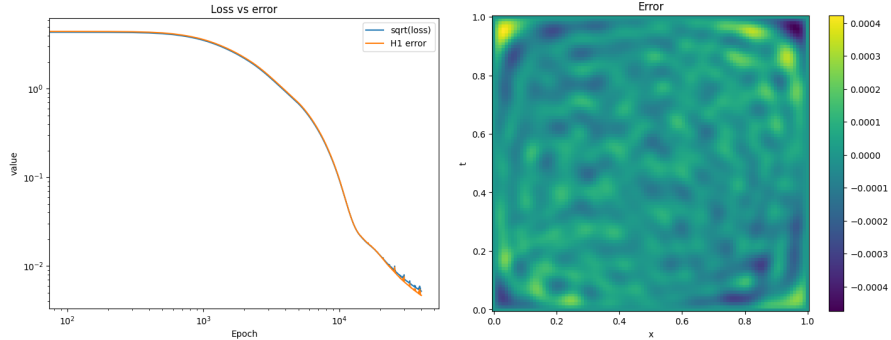


Figure 5: Robust CRVPINN convergence and error distribution.

We first switch to the ODIL method, where the neural network is replaced by a vector of coefficients $u_\theta = \{u_{i,j}\}$ and

$$R(u_\theta) = \sum_{x_{i,j}} \left(\frac{\partial u_{i,j}}{\partial x} + \frac{\partial u_{i,j}}{\partial y} + f_1(x_{i,j}) \right)^2. \quad (46)$$

Running ADAM optimizer with ODIL discretization using 100×100 collocation points takes 60,000 iterations, see Figure 6. It requires 90 sec of training in Google Compute Engine GPU, see Figure 7. Solving the ODIL method with Gauss-Newton based on a robust residual iterative solver takes 14.73 sec on Google Compute Engine GPU (28 times faster than CRVPINN). The ODIL

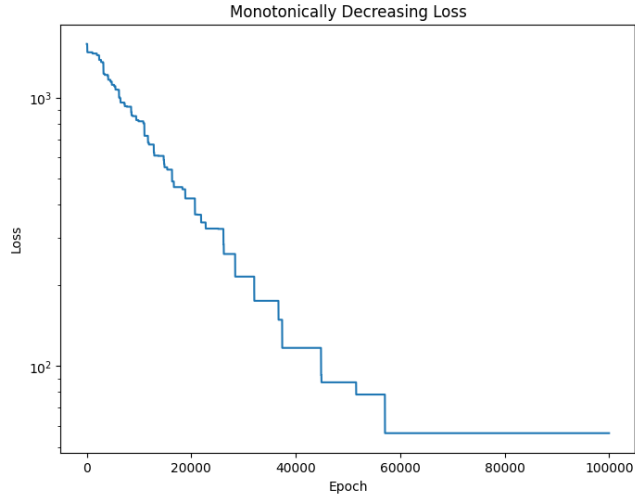


Figure 6: Convergence of ODIL training with ADAM method

loss is not robust and it is not related with the true error. The obtain L^2 norm accuracy is 0.00046.

Finally, we employ the IGA-ODIL approximation. IGA-ODIL replaces neural-network parameterizations with spline coefficients. The IGA-ODIL system is solved using the Gauss-Newton method. We employ MATLAB implementation, see Figure 8. We use 30×30 elements, cubic B-splines, and 30×30 collocation points. The resulting L^2 norm error is $6.468394e-04$. The Gauss-Newton

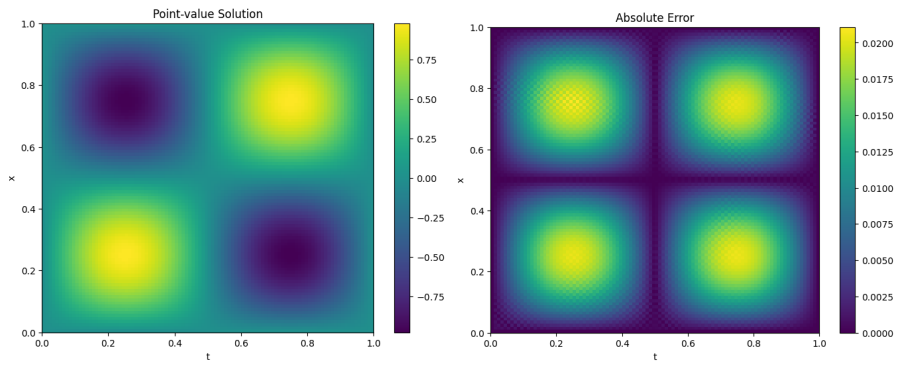


Figure 7: Solution obtained with ODIL method

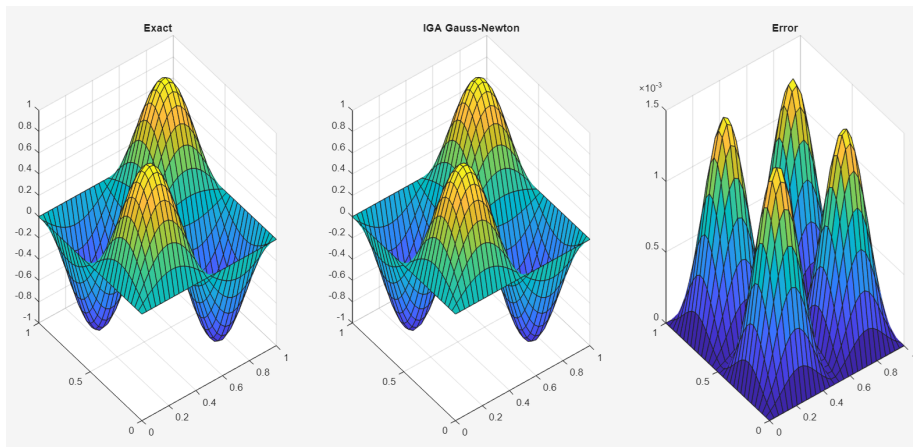


Figure 8: IGA-ODIL solution and error for the Poisson problem.

method takes 1 iteration and requires 0.04854 sec on MATLAB with a single core. More detailed evaluation of IGA-ODIL for different number of elements $n_x = n_y$, collocation points N_c and order p of B-splines which are C^{p-1} continuous is presented in Table 1 and Figure 9. In general, the accuracy increases with order of B-splines, provided there are enough collocation points. This is consistent with Theorem 1 presented in Appendix B. The IGA-ODIL is three orders of magnitude faster than CRVPINN.

5.2. Eriksson–Johnson Problem

To assess performance for convection-dominated regimes, we consider the Eriksson–Johnson advection–diffusion problem:

$$-\varepsilon \Delta u + \boldsymbol{\beta} \cdot \nabla u = 0, \quad (x, y) \in \Omega, \quad (47)$$

where $\varepsilon > 0$ is the diffusion coefficient and $\boldsymbol{\beta} = (1, 0)^T$ is the advection field. Boundary conditions are prescribed as:

$$u(0, y) = \sin(\pi y), \quad (\text{inflow}), \quad (48)$$

$$u(x, y) = 0, \quad \text{on remaining boundaries.} \quad (49)$$

For small values of ε , the solution exhibits boundary layers near the outflow boundary $x = 1$, making this a challenging benchmark for numerical methods.

Table 1: Results for the 2D Poisson problem solved with sparse IGA-ODIL.

p	$n_x = n_y$	N_c	Solver time [s]	L^2 error
1	10	30	4.618×10^{-4}	5.000×10^{-1}
1	20	30	3.922×10^{-4}	5.000×10^{-1}
1	30	30	3.450×10^{-4}	–
2	10	30	5.532×10^{-4}	5.187×10^{-3}
2	20	30	3.001×10^{-3}	2.700×10^{-3}
2	30	30	3.266×10^{-2}	9.704×10^{-3}
3	10	30	8.202×10^{-4}	6.324×10^{-4}
3	20	30	3.166×10^{-2}	1.162×10^{-4}
3	30	30	4.854×10^{-3}	6.468×10^{-4}

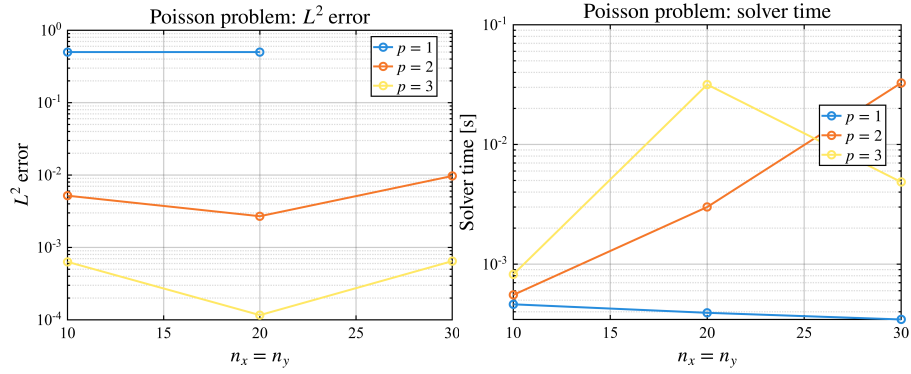


Figure 9: Accuracy and timing of IGA-ODIL solution for the Poisson problem for B-splines of order $p = 1, 2, 3$.

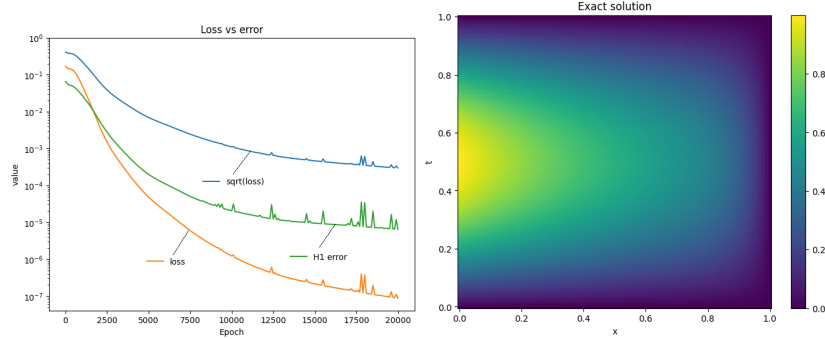


Figure 10: Advection-diffusion problem $\begin{cases} \beta \cdot \nabla u - \epsilon \Delta u = 0 & \text{in } \Omega, \\ u = g & \text{over } \partial\Omega. \end{cases}$

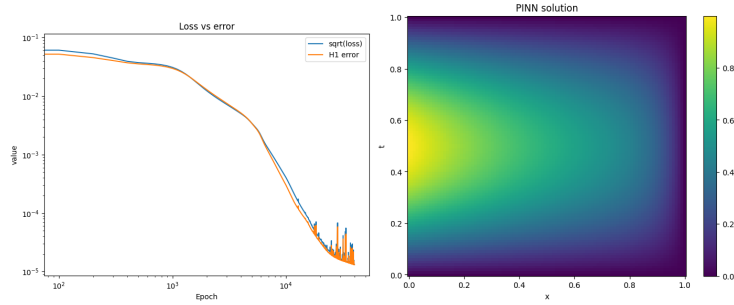


Figure 11: Advection-diffusion problem $\begin{cases} \beta \cdot \nabla u - \epsilon \Delta u = 0 & \text{in } \Omega, \\ u = g & \text{over } \partial\Omega. \end{cases}$

The problem exhibits the exact solution

$$u_{exact}(x, y) = \frac{(e^{r_1(x-1)} - e^{r_2(x-1)})}{(e^{-r_1} - e^{-r_2})} \sin(\pi y),$$

$$r_1 = \frac{(1 + \sqrt{(1 + 4\epsilon^2\pi^2)})}{(2\epsilon)}, r_2 = \frac{(1 - \sqrt{(1 + 4\epsilon^2\pi^2)})}{(2\epsilon)}. \quad (50)$$

Applying PINN for the Eriksson-Johnson problem for $\epsilon = 0.1$ results in a solution presented in Figure 10. The PINN loss is not robust. Upgrading to the robust loss as proposed by CRVPINN method, using 100×100 collocation points, two layers with 100 neurons, results in a solution presented in Figure 11. Total solution time on Google Compute Engine GPU is 3 min 31 sec.

Detailed evaluation of IGA-ODIL for $\epsilon = 0.001$, for different number of elements $n_x = n_y$, collocation points N_c and order p of B-splines which are C^{p-1} continuous is presented in Table 2 and Figure 12. In general, the accuracy

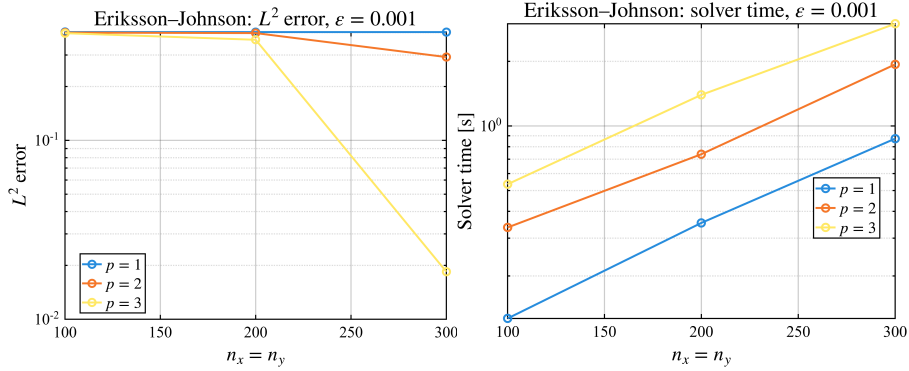


Figure 12: Accuracy and timing of IGA-ODIL solution for the Eriksson-Johnson problem for $\epsilon = 0.001$ for B-splines of order $p = 1, 2, 3$.

increases with order of B-splines, provided there are enough collocation points. This is consistent with theoretical estimate of Theorem 1 from Appendix B. The IGA-ODIL is two orders of magnitude faster than CRVPINN.

Table 2: Results for the Eriksson-Johnson problem with $\epsilon = 0.001$.

p	$n_x = n_y$	N_c	Solver time [s]	L^2 error
1	100	500	1.267×10^{-1}	4.032×10^{-1}
1	200	500	3.534×10^{-1}	4.031×10^{-1}
1	300	500	8.727×10^{-1}	4.031×10^{-1}
2	100	500	3.364×10^{-1}	4.004×10^{-1}
2	200	500	7.384×10^{-1}	3.978×10^{-1}
2	300	500	1.936×10^0	2.922×10^{-1}
3	100	500	5.351×10^{-1}	3.973×10^{-1}
3	200	500	1.396×10^0	3.651×10^{-1}
3	300	500	2.993×10^0	1.844×10^{-2}

5.3. Helmholtz Problem

We consider the Helmholtz problem:

$$-\Delta u + \alpha u = f, \quad (x, y) \in \Omega, \quad (51)$$

with homogeneous Dirichlet boundary conditions

$$u(x, y) = 0, \quad (x, y) \in \partial\Omega. \quad (52)$$

A manufactured solution is chosen as

$$u(x, y) = \sin(\kappa\pi x) \sin(\kappa\pi y), \quad (53)$$

where $\kappa \in \mathbb{N}$ controls the frequency. The corresponding forcing term is

$$f(x, y) = (2(\kappa\pi)^2 + \alpha) \sin(\kappa\pi x) \sin(\kappa\pi y). \quad (54)$$

This problem is particularly challenging for large values of κ due to oscillatory behavior and the well-known pollution effect. We set up the problem with $\kappa = 40$. PINN, CRVPINN, and ODIL methods fail to solve this difficult Helmholtz problem for $\kappa = 40$. IGA-ODIL successfully resolves oscillatory solutions with sparse Gauss-Newton optimization. We employ 80×80 elements, cubic B-splines, and 160×160 collocation points. The resulting accuracy in L^2 norm is $1.467537\text{e-}02$. The solution takes 0.15 sec on a MATLAB single core CPU.

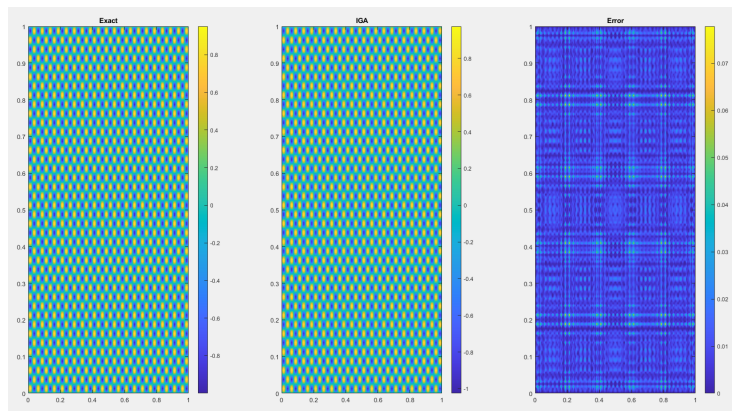


Figure 13: IGA-ODIL solution for the Helmholtz problem with $\kappa = 40$.

5.4. Three-Dimensional Helmholtz Problem

We further consider a three-dimensional Helmholtz benchmark, see Figure 14. We solve the problem for $\kappa = 10$ using $20 \times 20 \times 20$ elements, cubic B-splines,

$40 \times 40 \times 40$ collocation points, $\kappa = 10$, and the Gauss-Newton method. The resulting accuracy in L^2 norm is $1.902649\text{e-}02$. The problem takes 7.82 sec on a MATLAB single core CPU.

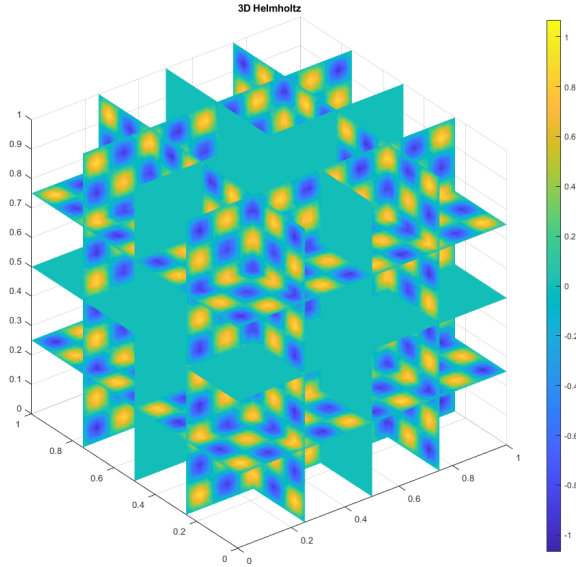


Figure 14: Three-dimensional Helmholtz solution obtained with IGA-ODIL.

5.5. Allen–Cahn Equation

We consider the steady Allen–Cahn equation:

$$-\varepsilon^2 \Delta u + (u^3 - u) = f, \quad (x, y) \in \Omega, \quad (55)$$

with Dirichlet boundary conditions

$$u(x, y) = g(x, y), \quad (x, y) \in \partial\Omega. \quad (56)$$

Using a manufactured solution

$$u(x, y) = \tanh\left(\frac{x + y - 1}{\sqrt{2}\varepsilon}\right), \quad (57)$$

the forcing term is given by

$$f(x, y) = \tanh\left(\frac{x + y - 1}{\sqrt{2}\varepsilon}\right) - \tanh^3\left(\frac{x + y - 1}{\sqrt{2}\varepsilon}\right). \quad (58)$$

The Allen–Cahn equation represents a nonlinear reaction–diffusion system exhibiting bistability and sharp interface layers for small values of ε , making it a suitable benchmark for nonlinear solvers. Detailed evaluation of IGA-ODIL for Allen-Cahn problem with $\varepsilon = 0.01$, for different number of elements $n_x = n_y$, collocation points N_c and order p of B-splines which are C^{p-1} continuous is presented in Table 3 and Figure 16. In general, the accuracy increases with number of elements, provided there are enough collocation points.

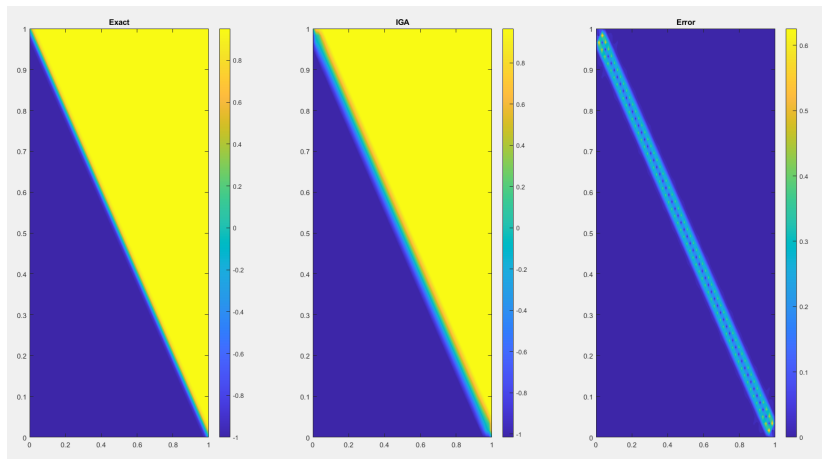


Figure 15: IGA-ODIL solution for the Allen–Cahn equation.

5.6. Eriksson–Johnson Problem on a Circular Domain

We consider the convection–diffusion equation posed on the unit disk $\Omega = \{(x, y) \in \mathbb{R}^2 : x^2 + y^2 \leq 1\}$, given by

$$-\varepsilon \Delta u + \boldsymbol{\beta} \cdot \nabla u = 0 \quad \text{in } \Omega, \quad (59)$$

where $\varepsilon > 0$ denotes the diffusion coefficient and $\boldsymbol{\beta} = (1, 0)^T$ is the convection direction. The computational domain is parameterized by a tensor-product spline space on the reference square $(\xi, \eta) \in [0, 1]^2$. To obtain a circular physical domain, we employ a smooth square-to-disk transformation. We first define

$$a = 2\xi - 1, \quad b = 2\eta - 1, \quad (60)$$

Table 3: Results for the Allen–Cahn problem solved with sparse IGA–ODIL/Newton iterations.

p	$n_x = n_y$	N_c	Time [s]	L^2 error
1	10	60	5.139×10^{-2}	2.155×10^{-1}
1	20	60	8.132×10^{-2}	1.085×10^{-1}
1	30	60	1.093×10^{-1}	6.421×10^{-2}
1	40	60	1.799×10^{-1}	4.750×10^{-2}
2	10	60	4.190×10^{-2}	2.076×10^{-1}
2	20	60	9.090×10^{-2}	1.069×10^{-1}
2	30	60	1.931×10^{-1}	7.879×10^{-2}
2	40	60	3.123×10^{-1}	8.191×10^{-2}
3	10	60	6.398×10^{-2}	2.071×10^{-1}
3	20	60	1.330×10^{-1}	1.046×10^{-1}
3	30	60	2.403×10^{-1}	7.824×10^{-2}
3	40	60	3.375×10^{-1}	8.594×10^{-2}

and then we introduce the mapping

$$x = a\sqrt{1 - \frac{b^2}{2}}, \quad y = b\sqrt{1 - \frac{a^2}{2}}. \quad (61)$$

This mapping transforms the unit square into the unit disk while avoiding the singularity associated with polar coordinates at the origin. In particular the mapping is smooth, and no coordinate singularity appears at the center. Additionally, tensor-product spline discretizations can still be used, and the collocation points remain structured in parameter space. The PDE is solved in the parametric domain, while the numerical solution is visualized on the physical circular geometry. The numerical solution is represented as

$$u_h(\xi, \eta) = \sum_{i=1}^{n_x} \sum_{j=1}^{n_y} c_{j,i} B_i(\xi) B_j(\eta), \quad (62)$$

where B_i and B_j are tensor-product B-spline basis functions. In the present

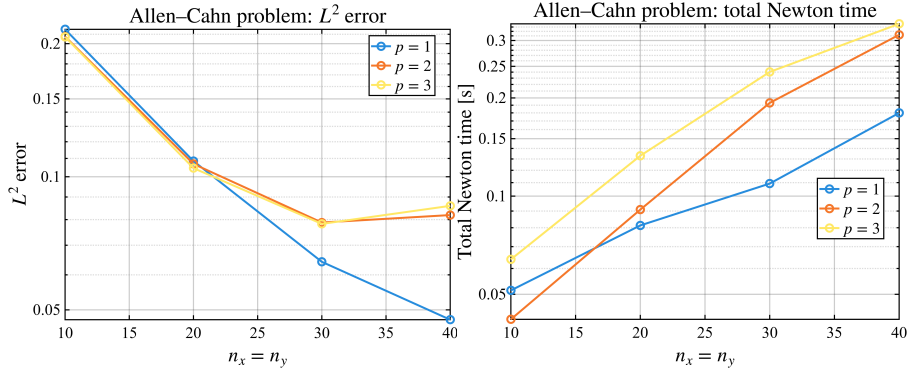


Figure 16: Accuracy and timing of IGA-ODIL solution for the Allen-Cahn problem for $\epsilon = 0.01$ for B-splines of order $p = 1, 2, 3$.

implementation, the strong-form residual is evaluated in parameter space:

$$R(u_h) = -\epsilon \left(\frac{\partial^2 u_h}{\partial \xi^2} + \frac{\partial^2 u_h}{\partial \eta^2} \right) + \frac{\partial u_h}{\partial \xi}. \quad (63)$$

The spline coefficients are obtained by minimizing the least-squares functional

$$\mathcal{J}(c) = \frac{1}{2} \sum_{k=1}^{N_c} |R(u_h)(\xi_k, \eta_k)|^2, \quad (64)$$

evaluated at collocation points $\{(\xi_k, \eta_k)\}_{k=1}^{N_c}$. Dirichlet boundary conditions are imposed strongly through elimination of boundary spline coefficients. The inflow boundary condition is prescribed on the left side of the parametric domain:

$$u(0, \eta) = \sin(\pi\eta), \quad (65)$$

while homogeneous conditions are imposed on the remaining boundaries. We use 40×40 elements and cubic B-splines with 200×200 collocation points for $\epsilon = 0.1$. The problem takes 0.15 sec on single core MATLAB with Gauss-Newton method. The solution is presented in Figure 17. This formulation demonstrates how residual minimization in spline spaces can naturally incorporate nontrivial geometric mappings while preserving the tensor-product structure of the discretization.

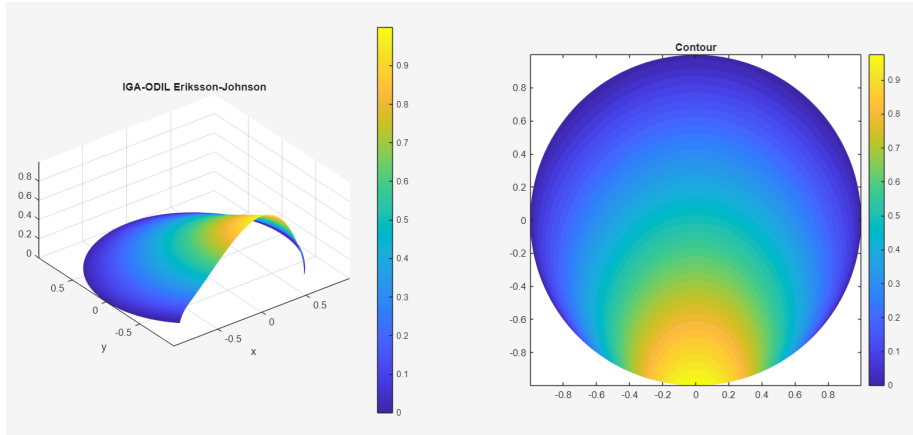


Figure 17: Eriksson-Johnson problem solved in a circular domain

5.7. Helmholtz Equation on a Ball

We next consider the three-dimensional Helmholtz equation posed on the unit ball $\Omega = \{(x, y, z) \in \mathbb{R}^3 : x^2 + y^2 + z^2 \leq 1\}$. The governing equation reads

$$-\Delta u + \kappa^2 u = f \quad \text{in } \Omega, \quad (66)$$

subject to homogeneous Dirichlet boundary conditions

$$u = 0 \quad \text{on } \partial\Omega. \quad (67)$$

The geometry of the ball is represented through a smooth mapping from the parametric cube $(\xi, \eta, \zeta) \in [0, 1]^3$ to the physical domain. Introducing $a = 2\xi - 1$, $b = 2\eta - 1$, $c = 2\zeta - 1$, the cube-to-ball transformation is defined by

$$x = a\sqrt{1 - \frac{b^2}{2} - \frac{c^2}{2} + \frac{b^2c^2}{3}}, \quad (68)$$

$$y = b\sqrt{1 - \frac{a^2}{2} - \frac{c^2}{2} + \frac{a^2c^2}{3}}, \quad (69)$$

$$z = c\sqrt{1 - \frac{a^2}{2} - \frac{b^2}{2} + \frac{a^2b^2}{3}}. \quad (70)$$

This mapping transforms the unit cube into a smooth approximation of the unit ball while preserving tensor-product spline parameterization. The approximate solution is represented in the parametric domain using tensor-product

B-splines:

$$u_h(\xi, \eta, \zeta) = \sum_{i=1}^{n_x} \sum_{j=1}^{n_y} \sum_{k=1}^{n_z} C_{ijk} B_i(\xi) B_j(\eta) B_k(\zeta), \quad (71)$$

where B_i , B_j , and B_k denote univariate B-spline basis functions. For verification purposes, we employ the manufactured solution

$$u(\xi, \eta, \zeta) = \sin(\kappa\pi\xi) \sin(\kappa\pi\eta) \sin(\kappa\pi\zeta), \quad (72)$$

which yields the forcing term

$$f(\xi, \eta, \zeta) = (3\kappa^2\pi^2 + \kappa^2) u(\xi, \eta, \zeta). \quad (73)$$

The residual minimization formulation is constructed directly in the parametric domain:

$$R(\xi, \eta, \zeta) = -\Delta_{\xi, \eta, \zeta} u_h + \kappa^2 u_h - f, \quad (74)$$

and the spline coefficients are obtained by minimizing the discrete least-squares functional

$$\mathcal{J}(C) = \frac{1}{2} \sum_{m=1}^{N_c} R(\xi_m, \eta_m, \zeta_m)^2, \quad (75)$$

evaluated at collocation points inside the parametric cube. The resulting linear system is solved after elimination of boundary degrees of freedom corresponding to the cube boundary, which maps onto the spherical boundary in physical space. First we use $16 \times 16 \times 16$ elements and cubic B-splines with $30 \times 30 \times 30$ collocation points for $\kappa = 6$. The problem takes 0.74 sec on single core MATLAB with Gauss-Newton method. The accuracy in L^2 norm is 5.425967e-03. Figure 18 presents multi-slice visualizations of the numerical solution inside the ball geometry. The smooth spline representation accurately resolves oscillatory Helmholtz modes while preserving geometric regularity of the mapped domain.

Second, we use $32 \times 32 \times 32$ elements with cubic B-splines with $64 \times 64 \times 64$ collocation points for $\kappa = 20$. The problem takes 23.43 sec on single core MATLAB with Gauss-Newton method. The resulting accuracy in L^2 norm is 4.742797e-02. This problem solution is illustrated in Figure 19.

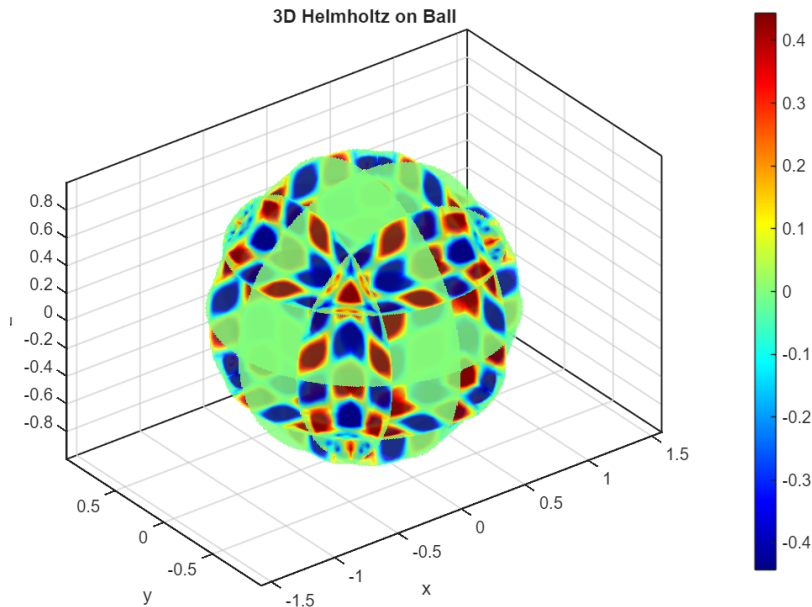


Figure 18: Multi-slice visualization of the 3D Helmholtz solution inside the mapped ball geometry using cubic B-splines and residual minimization. $16 \times 16 \times 16$ elements and cubic B-splines with $30 \times 30 \times 30$ collocation points for $\kappa = 6$.

6. Inverse Problems

IGA-ODIL naturally extends to PDE-constrained inverse problems due to its residual-based optimization formulation. In contrast to classical finite element approaches, where inverse problems often require repeated nested forward PDE solves, the proposed framework simultaneously optimizes both the state variables and unknown physical parameters within a unified optimization procedure. We consider inverse identification of parameters in the Helmholtz equation:

$$-\Delta u + \alpha u = f, \quad (x, y) \in \Omega, \quad (76)$$

subject to homogeneous Dirichlet boundary conditions

$$u(x, y) = 0, \quad (x, y) \in \partial\Omega. \quad (77)$$

A manufactured solution is prescribed as

$$u(x, y) = \sin(\kappa_{\text{true}}\pi x) \sin(\kappa_{\text{true}}\pi y), \quad (78)$$

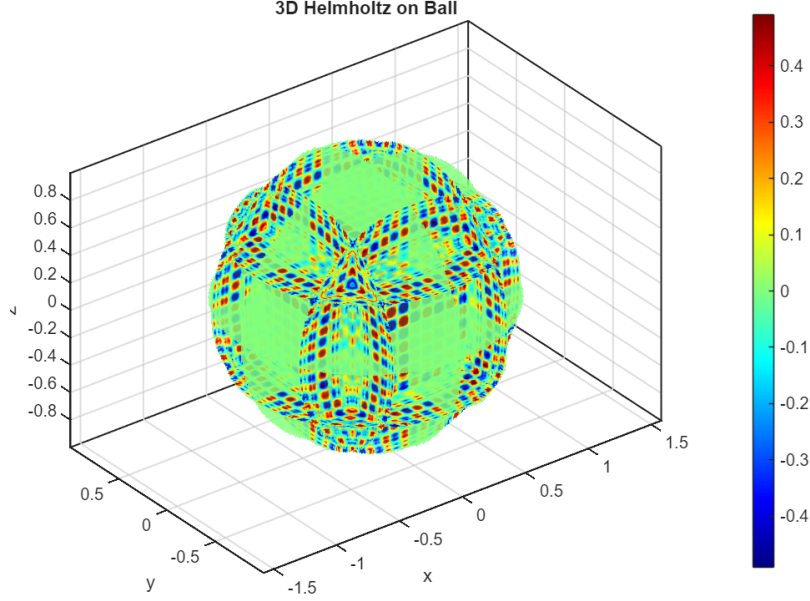


Figure 19: Multi-slice visualization of the 3D Helmholtz solution inside the mapped ball geometry using cubic B-splines and residual minimization. $32 \times 32 \times 32$ elements and cubic B-splines with $64 \times 64 \times 64$ collocation points for $\kappa = 20$.

where κ_{true} denotes the unknown frequency parameter to be recovered. The corresponding forcing term becomes

$$f(x, y) = (2(\kappa_{\text{true}}\pi)^2 + \alpha) \sin(\kappa_{\text{true}}\pi x) \sin(\kappa_{\text{true}}\pi y). \quad (79)$$

The objective of the inverse problem is to recover the unknown parameter κ from observations of the solution field.

6.1. IGA-ODIL Formulation for Inverse Problems

The spline approximation is written as

$$u_c(x, y) = \sum_{i=1}^{N_x} \sum_{j=1}^{N_y} c_{ij} B_i^{(p)}(x) B_j^{(q)}(y). \quad (80)$$

The inverse optimization problem is formulated as

$$\min_{c, \kappa} (\|R(c, \kappa)\|^2 + \lambda \|u_c - u_{\text{obs}}\|^2), \quad (81)$$

where $\lambda > 0$ is a regularization parameter and u_{obs} denotes observed solution data. The spline coefficients c_{ij} and parameter κ are optimized simultaneously. The residual is given by

$$R_k(c, \kappa) = -\Delta u_c(x_k, y_k) + \kappa^2 u_c(x_k, y_k) - f(x_k, y_k). \quad (82)$$

Expanding the spline representation yields

$$R_k(c, \kappa) = \sum_{i,j} c_{ij} \left[-\frac{\partial^2 B_i^{(p)}(x_k)}{\partial x^2} B_j^{(q)}(y_k) - B_i^{(p)}(x_k) \frac{\partial^2 B_j^{(q)}(y_k)}{\partial y^2} + \kappa^2 B_i^{(p)}(x_k) B_j^{(q)}(y_k) \right] - f(x_k, y_k). \quad (83)$$

The data misfit term becomes

$$\|u_c - u_{\text{obs}}\|^2 = \sum_k (u_c(x_k, y_k) - u_{\text{obs}}(x_k, y_k))^2. \quad (84)$$

The complete optimization functional is therefore

$$\Phi(c, \kappa) = \frac{1}{2} \sum_k R_k(c, \kappa)^2 + \frac{\lambda}{2} \sum_k (u_c(x_k, y_k) - u_{\text{obs}}(x_k, y_k))^2. \quad (85)$$

6.2. Gauss-Newton Linearization

Let

$$\theta = \begin{bmatrix} c \\ \kappa \end{bmatrix} \quad (86)$$

denote the vector of optimization variables. The residual vector is linearized as

$$R(\theta + \delta\theta) \approx R(\theta) + J(\theta)\delta\theta, \quad (87)$$

where

$$J(\theta) = \frac{\partial R}{\partial \theta} \quad (88)$$

is the Jacobian matrix. The Gauss-Newton system becomes

$$J^T J \delta\theta = -J^T R. \quad (89)$$

Due to the local support of B-spline basis functions, the Jacobian remains sparse with respect to spline coefficients. The additional parameter κ introduces only one dense column corresponding to

$$\frac{\partial R_k}{\partial \kappa} = 2\kappa u_c(x_k, y_k). \quad (90)$$

Consequently, the resulting system preserves favorable sparsity properties and remains computationally tractable.

6.3. Numerical Results

We first consider the recovery of the parameter $\kappa_{\text{true}} = 2.0$ starting from the initial guess $\kappa_{\text{initial}} = 1.0$. The computation employs 30×30 elements, cubic B-splines, 40×40 collocation points, and 100 Gauss–Newton iterations. Figure 20 illustrates the convergence of the recovered parameter. The corresponding reconstructed solution is shown in Figure 21.

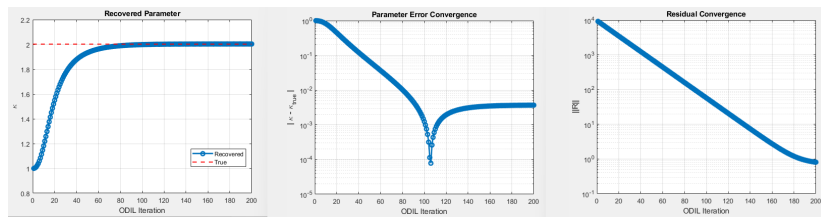


Figure 20: Convergence of inverse Helmholtz parameter recovery for $\kappa_{\text{true}} = 2$.

The parameter converges rapidly toward the exact value while the residual decreases monotonically. We next consider a substantially more oscillatory regime with $\kappa_{\text{true}} = 8$. The computational setup uses 40×40 spline elements, cubic B-splines, 80×80 collocation points, and 100 Gauss–Newton iterations. Figure 22 presents the convergence histories for the recovered parameter. The reconstructed oscillatory solution is shown in Figure 23.

Even in highly oscillatory regimes, the proposed formulation successfully recovers both the parameter and solution field. The computational time is approximately 9.8 seconds for $\kappa = 2$, and 59 seconds for $\kappa = 8$, on a single CPU core in MATLAB. These results demonstrate that IGA–ODIL naturally extends

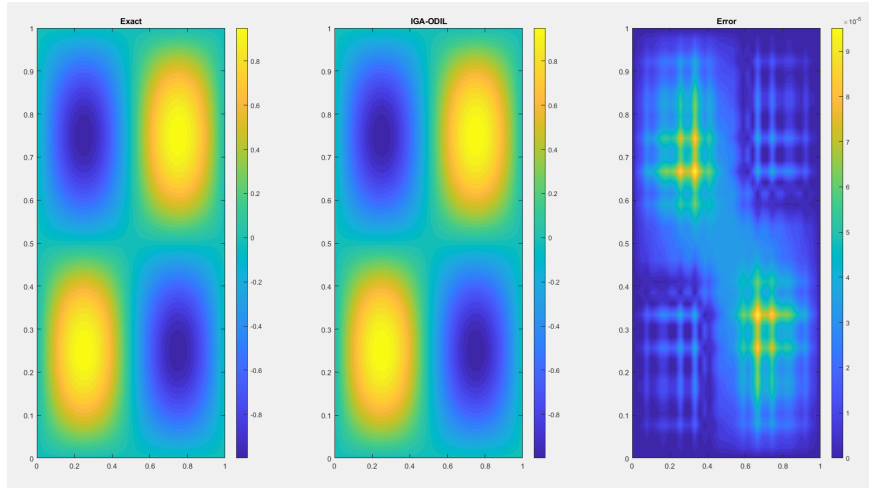


Figure 21: Recovered Helmholtz solution for $\kappa_{\text{true}} = 2$.

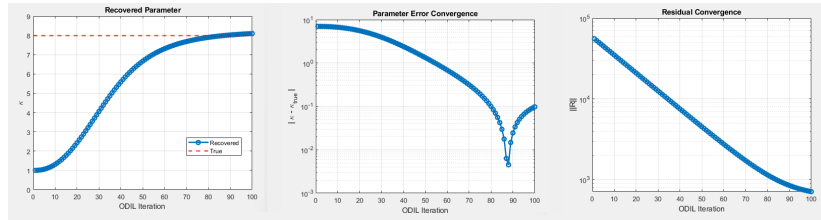


Figure 22: Convergence of inverse Helmholtz parameter recovery for $\kappa_{\text{true}} = 8$.

to PDE-constrained inverse problems while preserving the favorable sparsity and optimization properties of the forward formulation.

7. Conclusions

The proposed IGA-ODIL framework bridges scientific machine learning and classical numerical PDE discretization theory. The key conceptual observation is that residual minimization becomes computationally tractable when combined with structured spline parameterizations. The numerical experiments demonstrate that the proposed method provides a simple and flexible framework for solving a wide range of PDEs. By operating directly on the strong form of the governing equations, the method avoids the need for variational formulations

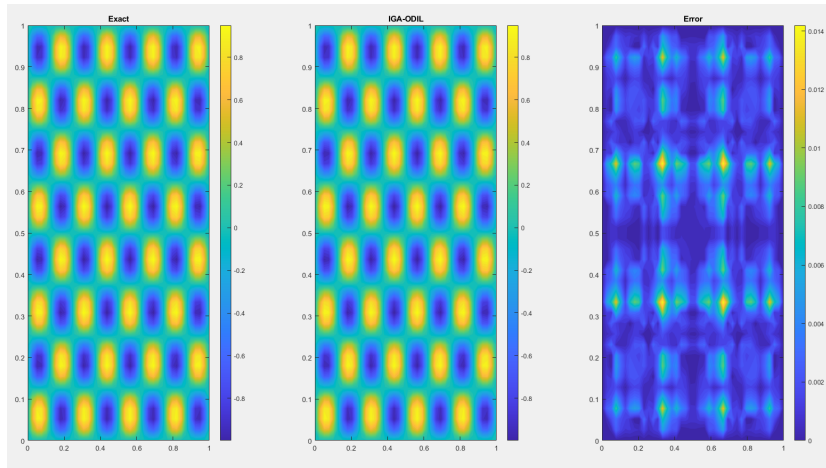


Figure 23: Recovered Helmholtz solution for $\kappa_{\text{true}} = 8$.

and numerical quadrature, which simplifies implementation compared to classical Galerkin-based approaches. The use of spline basis functions yields smooth approximations with high-order continuity, enabling accurate evaluation of differential operators and reducing the number of degrees of freedom required for a given accuracy. This is particularly advantageous for problems involving higher-order derivatives or smooth solutions. Furthermore, the formulation naturally leads to a least-squares problem with a structured Jacobian, allowing the use of efficient Gauss–Newton or Newton-type solvers. For linear problems, the method reduces to a single linear solve, while for nonlinear problems, it exhibits rapid (often quadratic) convergence under standard assumptions.

The proposed framework is closely related to least-squares finite element methods (LSFEM) [17], but differs in the choice of approximation space. While LSFEM typically employs low-order polynomial basis functions, the present approach utilizes smooth spline spaces from isogeometric analysis, leading to improved approximation properties. Compared to classical isogeometric Galerkin methods [14], the present formulation eliminates the need for weak forms and numerical integration, providing a more direct residual-based approach. However, this also implies that the method inherits some characteristics of collocation-

type methods. In contrast to physics-informed neural networks (PINNs) [1], the method uses a deterministic basis representation with a structured Jacobian, resulting in improved conditioning, reproducibility, and convergence behavior. The IGA-ODIL differs from the ODIL method [13] since it uses spline combination instead of discrete point values for training (optimization).

Despite its advantages, the proposed method has several limitations that warrant further investigation. First, the use of strong-form residuals requires sufficient regularity of the exact solution, as the differential operator is applied directly to the approximate solution. This may limit applicability to problems with low regularity or discontinuities. Second, the collocation-based approximation of the residual introduces a dependence on the choice and distribution of collocation points. While uniform grids perform well for smooth problems, more complex geometries or localized features may require adaptive sampling strategies. Third, for convection-dominated problems with very small diffusion coefficients, additional stabilization mechanisms or weighted residual formulations may be necessary to fully resolve sharp boundary layers without oscillations. Fourth, the formation of the Jacobian matrix can be computationally expensive for large-scale problems, particularly in higher dimensions. Although the structure of the spline basis can be exploited, further work is needed to develop efficient matrix-free or low-rank implementations. Finally, while Gauss-Newton iterations perform well in the examples considered, global convergence is not guaranteed for strongly nonlinear problems. In such cases, damping strategies or line search techniques may be required.

Appendix A. Code availability

The MATLAB codes employed in the paper to solve IGA-ODIL problems are available at

`https://github.com/sluzalec/IGA-ODIL`

The Python codes used for running PINN and CRVPINN experiments are available in paper [12].

Appendix B. Convergence of IGA-ODIL

Theorem 1 (Convergence of robust spline-based residual minimization). *Let $\Omega \subset \mathbb{R}^d$ be a bounded Lipschitz domain, and consider the boundary value problem*

$$\mathcal{L}u = f \quad \text{in } \Omega, \quad (\text{B.1})$$

supplemented with boundary conditions such that the problem is well posed.

Assume that:

1. $\mathcal{L} : H^m(\Omega) \rightarrow L^2(\Omega)$ is a linear differential operator of order $s \leq m$.
2. The exact solution satisfies $u \in H^{p+1}(\Omega)$.
3. The spline approximation space $V_h \subset H^m(\Omega)$ consists of tensor-product B-splines of degree p constructed on a quasi-uniform mesh with characteristic size h .
4. The collocation points $\mathcal{X}_M = \{x_k\}_{k=1}^M \subset \Omega$ are quasi-uniform with fill distance $h_c := \sup_{x \in \Omega} \min_{x_k \in \mathcal{X}_M} \|x - x_k\|$, satisfying $h_c \lesssim h$.
5. The discrete robust residual minimization problem

$$u_h = \arg \min_{v_h \in V_h} \Phi_h(v_h) \quad (\text{B.2})$$

is defined by the functional

$$\Phi_h(v_h) = \frac{1}{2} R(v_h)^T G^{-1} R(v_h), \quad (\text{B.3})$$

where

$$R(v_h) = [\mathcal{L}v_h(x_1) - f(x_1), \dots, \mathcal{L}v_h(x_M) - f(x_M)]^T \in \mathbb{R}^M, \quad (\text{B.4})$$

and $G \in \mathbb{R}^{M \times M}$ is a symmetric positive definite Gram matrix.

6. The operator \mathcal{L} satisfies the stability estimate

$$\|w\|_{H^m(\Omega)} \leq C_{\text{stab}} \|\mathcal{L}w\|_{L^2(\Omega)} \quad \forall w \in H_0^m(\Omega). \quad (\text{B.5})$$

7. The collocation sampling satisfies the norm equivalence

$$\|v_h\|_{L^2(\Omega)}^2 \sim \sum_{k=1}^M |v_h(x_k)|^2 \quad \forall v_h \in V_h, \quad (\text{B.6})$$

with constants independent of h .

8. The Gram matrix induces a uniformly equivalent discrete norm:

$$c_G \|r\|_2^2 \leq r^T G^{-1} r \leq C_G \|r\|_2^2 \quad \forall r \in \mathbb{R}^M, \quad (\text{B.7})$$

with constants independent of h .

Then the robust IGA-ODIL approximation satisfies the error estimate

$$\|u - u_h\|_{H^m(\Omega)} \leq C \|R(u_h)\|_G, \quad (\text{B.8})$$

where

$$\|R(u_h)\|_G := (R(u_h)^T G^{-1} R(u_h))^{1/2}. \quad (\text{B.9})$$

Moreover,

$$\|R(u_h)\|_G \leq Ch^{p+1-s} |u|_{H^{p+1}(\Omega)}, \quad (\text{B.10})$$

and therefore

$$\|u - u_h\|_{H^m(\Omega)} = \mathcal{O}(h^{p+1-s}). \quad (\text{B.11})$$

Proof. Step 1: Spline approximation property.

Since $u \in H^{p+1}(\Omega)$, classical spline approximation theory (cf. Ciarlet [27], Schumaker [28], Bazilevs et al. [29]) implies the existence of a spline interpolant $\Pi_h u \in V_h$ such that

$$\|u - \Pi_h u\|_{H^m(\Omega)} \leq Ch^{p+1-m} |u|_{H^{p+1}(\Omega)}. \quad (\text{B.12})$$

Since \mathcal{L} is a differential operator of order s , standard continuity estimates yield

$$\|\mathcal{L}(u - \Pi_h u)\|_{L^2(\Omega)} \leq Ch^{p+1-s} |u|_{H^{p+1}(\Omega)}. \quad (\text{B.13})$$

Step 2: Minimality of the robust residual functional.

Since $u_h = \arg \min_{v_h \in V_h} \Phi_h(v_h)$, we have

$$\Phi_h(u_h) \leq \Phi_h(\Pi_h u). \quad (\text{B.14})$$

Using the definition of the robust functional, $\Phi_h(v_h) = \frac{1}{2} R(v_h)^T G^{-1} R(v_h)$, this becomes

$$R(u_h)^T G^{-1} R(u_h) \leq R(\Pi_h u)^T G^{-1} R(\Pi_h u). \quad (\text{B.15})$$

Since the exact solution satisfies $\mathcal{L}u = f$, the residual associated with the interpolant satisfies $R(\Pi_h u) = [\mathcal{L}(\Pi_h u - u)(x_k)]_{k=1}^M$.

Using the Gram norm equivalence (B.7),

$$R(\Pi_h u)^T G^{-1} R(\Pi_h u) \leq C_G \sum_{k=1}^M |\mathcal{L}(\Pi_h u - u)(x_k)|^2. \quad (\text{B.16})$$

Applying the sampling equivalence (B.6),

$$\sum_{k=1}^M |\mathcal{L}(\Pi_h u - u)(x_k)|^2 \leq C \|\mathcal{L}(\Pi_h u - u)\|_{L^2(\Omega)}^2. \quad (\text{B.17})$$

Combining (B.13), (B.16), and (B.17) yields

$$R(u_h)^T G^{-1} R(u_h) \leq Ch^{2(p+1-s)} |u|_{H^{p+1}(\Omega)}^2. \quad (\text{B.18})$$

Taking square roots gives

$$\|R(u_h)\|_G \leq Ch^{p+1-s} |u|_{H^{p+1}(\Omega)}. \quad (\text{B.19})$$

This proves (B.10).

Step 3: Stability estimate.

Define the approximation error $e_h := u - u_h$. Using linearity of the operator, $\mathcal{L}e_h = f - \mathcal{L}u_h$. Applying the stability estimate (B.5),

$$\|e_h\|_{H^m(\Omega)} \leq C_{\text{stab}} \|f - \mathcal{L}u_h\|_{L^2(\Omega)}. \quad (\text{B.20})$$

Using the sampling equivalence,

$$\|f - \mathcal{L}u_h\|_{L^2(\Omega)}^2 \sim \sum_{k=1}^M |\mathcal{L}u_h(x_k) - f(x_k)|^2. \quad (\text{B.21})$$

Applying the Gram equivalence (B.7),

$$\sum_{k=1}^M |\mathcal{L}u_h(x_k) - f(x_k)|^2 \leq c_G^{-1} R(u_h)^T G^{-1} R(u_h). \quad (\text{B.22})$$

Therefore,

$$\|f - \mathcal{L}u_h\|_{L^2(\Omega)} \leq C \|R(u_h)\|_G. \quad (\text{B.23})$$

Substituting into (B.20) gives

$$\|u - u_h\|_{H^m(\Omega)} \leq C \|R(u_h)\|_G. \quad (\text{B.24})$$

Finally, combining (B.24) with (B.19) yields

$$\|u - u_h\|_{H^m(\Omega)} \leq Ch^{p+1-s} |u|_{H^{p+1}(\Omega)}. \quad (\text{B.25})$$

Hence, $\|u - u_h\|_{H^m(\Omega)} = \mathcal{O}(h^{p+1-s})$, which proves (B.11).

□

Acknowledgments This work has been supported by the National Science Centre, Poland grant no. 2025/57/B/ST6/00058. This work has received funding from the European Union’s Horizon Europe research and innovation programme under the Marie Skłodowska-Curie grant agreement No 101119556. The authors are grateful for the support from the funds that the Polish Ministry of Science and Higher Education assigned to AGH University of Krakow. The work is supported by the “Excellence initiative - research university” for AGH University of Krakow.

Declaration of Generative AI and AI-assisted technologies in the writing process During the preparation of this work, the author(s) used ChatGPT to assist with writing, correct English language usage, and improve text clarity and organization. After using this tool/service, the author(s) reviewed and edited the content as needed and take(s) full responsibility for the content of the publication.

References

- [1] M. Raissi, P. Perdikaris, G. E. Karniadakis, Physics-informed neural networks: A deep learning framework for solving forward and inverse problems involving nonlinear partial differential equations, *Journal of Computational Physics*, 378 (2019) 686–707.
- [2] S. Cai, Z. Mao, Z. Wang, M. Yin, G. E. Karniadakis, Physics-informed neural networks (PINNs) for fluid mechanics: A review, *Acta Mechanica Sinica*, 37 (2021) 1727–1738.
- [3] J. Xu, H. Wei, H. Bao, Physics-informed neural networks for studying heat transfer in porous media, *International Journal of Heat and Mass Transfer*, 217 (2023) 124671.
- [4] D. Jalili, S. Jang, M. Jadidi, G. Giustini, A. Keshmiri, Y. Mahmoudi, Physics-informed neural networks for heat transfer prediction in two-phase flows, *International Journal of Heat and Mass Transfer*, 221 (2024) 125089.
- [5] S. Yang, H. Kim, Y. Hong, K. Yee, R. Maulik, N. Kang, Data-driven physics-informed neural networks: A digital twin perspective, *Computer Methods in Applied Mechanics and Engineering*, 428 (2024) 117075.
- [6] L. Zhu, X. Jiang, A. Lefauve, R. R. Kerswell, P. F. Linden, New insights into experimental stratified flows obtained through physics-informed neural networks, *Journal of Fluid Mechanics*, 981 (2024) R1.
- [7] Z. Zhao, Y. Wang, W. Zhang, Z. Ba, L. Sun, Physics-informed neural networks in heat transfer-dominated engineering applications, *Engineering Applications of Artificial Intelligence*, (2025).
- [8] S. Wang, Y. Teng, P. Perdikaris, Understanding and mitigating gradient flow pathologies in physics-informed neural networks, *SIAM Journal on Scientific Computing*, 43 (2021) A3055–A3081.

- [9] E. Kharazmi, Z. Zhang, G. E. Karniadakis, hp-VPINNs: Variational physics-informed neural networks with domain decomposition, *Computer Methods in Applied Mechanics and Engineering*, 374 (2021) 113547.
- [10] E. Weinan, B. Yu, The Deep Ritz method: A deep learning-based numerical algorithm for solving variational problems, *Communications in Mathematics and Statistics*, 6 (2018) 1–12.
- [11] S. Rojas, P. Maczuga, J. Muñoz-Matute, D. Pardo, M. Paszyński, Robust Variational Physics-Informed Neural Networks, *Computer Methods in Applied Mechanics and Engineering*, 425 (2024) 116902.
- [12] M. Łoś, T. Służalec, P. Maczuga, A. Vilka, C. Uriarte, M. Paszyński, Collocation-based Robust Variational Physics-Informed Neural Networks (CRVPINN), *Computers and Structures*, 316 (2025) 107904.
- [13] P. Karnakov, S. Litvinov, P. Koumoutsakos, Solving inverse problems in physics by optimizing a discrete loss: Fast and accurate learning without neural networks, *PNAS Nexus*, 3 (2024) pgae005.
- [14] T. J. R. Hughes, J. A. Cottrell, Y. Bazilevs, Isogeometric analysis: CAD, finite elements, NURBS, exact geometry and mesh refinement, *Computer Methods in Applied Mechanics and Engineering*, 194 (2005) 4135–4195.
- [15] J. A. Cottrell, T. J. R. Hughes, Y. Bazilevs, *Isogeometric Analysis: Toward Integration of CAD and FEA*, Wiley, 2009.
- [16] Y. Bazilevs, L. Beirão da Veiga, J. A. Cottrell, T. J. R. Hughes, G. Sangalli, Isogeometric analysis: Approximation, stability and error estimates for h -refined meshes, *Mathematical Models and Methods in Applied Sciences*, 16 (2006) 1031–1090.
- [17] P. Bochev, M. Gunzburger, *Least-Squares Finite Element Methods*, Springer, 2009.

- [18] A. Quarteroni, A. Valli, *Numerical Approximation of Partial Differential Equations*, Springer, 1994.
- [19] J. Nocedal, S. Wright, *Numerical Optimization*, Springer, 2006.
- [20] G. E. Karniadakis, I. Kevrekidis, L. Lu, P. Perdikaris, S. Wang, L. Yang, Physics-informed machine learning, *Nature Reviews Physics*, 3 (2021) 422–440.
- [21] Z. Li, N. Kovachki, K. Azizzadenesheli, B. Liu, K. Bhattacharya, A. Stuart, A. Anandkumar, Fourier neural operator for parametric partial differential equations, *arXiv preprint*, arXiv:2010.08895, 2020.
- [22] M. Hinze, R. Pinnau, M. Ulbrich, S. Ulbrich, *Optimization with PDE Constraints*, Springer, 2009.
- [23] T. J. R. Hughes, L. Franca, G. Scovazzi, Multiscale and stabilized methods, in: *Encyclopedia of Computational Mechanics*, 2004.
- [24] D. P. Kingma, J. Ba, Adam: A method for stochastic optimization, *arXiv preprint*, arXiv:1412.6980, 2014.
- [25] T. J. R. Hughes, G. Sangalli, T. Takacs, D. Toshniwal, Smooth multi-patch discretizations in isogeometric analysis, *Handbook of Numerical Analysis*, 22 (2021) 467–543.
- [26] A. Buffa, G. Sangalli, R. Vázquez, Isogeometric methods for computational electromagnetics: B-spline and T-spline discretizations, *Journal of Computational Physics*, 257 (2014) 1291–1320.
- [27] P. G. Ciarlet, *The Finite Element Method for Elliptic Problems*, SIAM, Philadelphia, 2002.
- [28] L. L. Schumaker, *Spline Functions: Basic Theory*, 3rd ed., Cambridge University Press, Cambridge, 2007.

- [29] Y. Bazilevs, L. Beirão da Veiga, J. A. Cottrell, T. J. R. Hughes, G. Sangalli, Isogeometric analysis: Approximation, stability and error estimates for h -refined meshes, *Mathematical Models and Methods in Applied Sciences*, 17 (2006) 1031–1090.
- [30] L. Chen, B. Li, R. de Borst, Adaptive isogeometric analysis for phase-field modeling of anisotropic brittle fracture, *International Journal for Numerical Methods in Engineering*, 121 (2020) 4630–4648.
- [31] S. Goswami, C. Anitescu, T. Rabczuk, Adaptive fourth-order phase field analysis for brittle fracture, *Computer Methods in Applied Mechanics and Engineering*, 361 (2020) 112808.
- [32] N. Nguyen-Thanh, W. Li, J. Huang, K. Zhou, Adaptive higher-order phase-field modeling of anisotropic brittle fracture in 3D polycrystalline materials, *Computer Methods in Applied Mechanics and Engineering*, 372 (2020) 113434.
- [33] J. Gao, M. Xiao, Y. Zhang, L. Gao, A comprehensive review of isogeometric topology optimization: Methods, applications and prospects, *Chinese Journal of Mechanical Engineering*, 33 (2020) 87.
- [34] X. Wei, X. Li, K. Qian, T. J. R. Hughes, Y. J. Zhang, H. Casquero, Analysis-suitable unstructured T-splines: Multiple extraordinary points per face, *Computer Methods in Applied Mechanics and Engineering*, 391 (2022) 114494.
- [35] Z. Wen, M. S. Faruque, X. Li, X. Wei, H. Casquero, Isogeometric analysis using G-spline surfaces with arbitrary unstructured quadrilateral layout, *Computer Methods in Applied Mechanics and Engineering*, 408 (2023) 115965.
- [36] Y. Bazilevs, K. Takizawa, T. E. Tezduyar, A. Korobenko, T. Kuraishi, Y. Otoguro, Computational aerodynamics with isogeometric analysis, *Journal of Mechanics*, 39 (2023) 24–39.

- [37] M. Torre, S. Morganti, F. S. Pasqualini, A. Reali, Current progress toward isogeometric modeling of the heart biophysics, *Biophysics Reviews*, 4 (2023) 041301.
- [38] L. Greco, A. Patton, M. Negri, A. Marengo, U. Perego, A. Reali, Higher order phase-field modeling of brittle fracture via isogeometric analysis, *Engineering with Computers*, 40 (2024) 3541–3560.
- [39] R. Willems, K. L. P. M. Janssens, P. H. M. Bovendeerd, C. V. Verhoosel, O. van der Sluis, An isogeometric analysis framework for ventricular cardiac mechanics, *Computational Mechanics*, 73 (2024) 465–506.
- [40] T. Kuraishi, Z. Xu, K. Takizawa, T. E. Tezduyar, T. Kakegami, Space–time isogeometric analysis of tire aerodynamics with complex tread pattern, road contact, and tire deformation, *Computational Mechanics*, 75 (2025) 575–591.